Fully Configurable Electromagnetic Wave Absorbers by Using Carbon Nanostructures

Davide Micheli, Roberto Pastore,
Antonio Vricella and Mario Marchetti

Additional information is available at the end of the chapter

Abstract

The configurable electromagnetic wave absorber (CEMA) defines a new method for the full design of layered carbon-based nanocomposites able to quasi-perfectly reproduce any kind of EM reflection coefficient (RC) profile. The method involves three main factors: (a) nanofillers-like carbon nanotube (CNT), carbon nanofiber (CNF), graphene nanoplatelet (GNP), and polyaniline (PANI) in different concentration versus the matrix; (b) the dielectric parameters of the nanoreinforced materials in the microwave range 2–18 GHz; (c) a numerical technique based on particle swarm optimization (PSO) algorithm within the MATLAB code of the EM propagation engine. Output is the layering of the wave absorber, that is, number of layers and material/thickness of each layer and the reflection/transmission simulated profiles. The frequency selective behavior is due to the multilayered composition, thanks to the direct/reflected wave combination tuning at interfaces. The dielectric characterization of the employed nanocomposites is presented in details: these materials constitute the database for the optimization code running toward the multilayer optimal solution. A FEM analysis is further proposed to highlight the EM propagation within the material's bulk at different frequencies. The mathematical model of layered materials, the PSO objective function used for RC target fitting, and some results are reported in the text.

Keywords: carbon nanoparticles, particle swarm optimization, layered electromagnetic wave absorber, nanocomposite materials

1. Introduction

In the last 50 years, many research activities have been focused on materials and structures able to reduce the electromagnetic reflection coefficient (RC) in certain frequency ranges.

Applications are mostly in military technology, with radar absorbing materials (RAM) and radar absorbing structure (RAS) [1–6], and in electromagnetic compatibility (EMC) for EM shielding and EM interference (EMI) suppression purposes [7–9], as well as for antenna testing in anechoic chambers [10, 11]. Nowadays, the increase of wireless communication systems demands the use of specific technologies or technical solutions to reduce the mutual telecommunication (TLC) systems interference. In fact, in order to reduce the energy impact and the constraints imposed by cost savings, most different wireless systems are often co-located in the same place, that is, sharing the same basic infrastructures. The proximity of such TLC systems can give rise to mutual radio frequency (RF) interferences due to intermodulation products in the shared antenna systems and/or to low efficiency in filtering out the spurious RF components. In this complex context, the availability of a new kind of materials, able to be frequency selective, absorbing, and tunable, is particularly attractive to reduce mutual EMI issues in specific frequency ranges [12]. Another field where configurable EM wave absorbers appear useful is the metrological science and technology. For example, in remote sensing, operations are sometimes necessary to often verify the sensors capability to detect and recognize certain material signatures on the Earth surface [13, 14]. Such type of testing and better sensors and algorithms calibration could be easily tuned in situ by using standard metrological samples, able to reproduce the desired EM target signatures. Further applications of tunable EM wave absorbers are conceivable in the security field. Nowadays, some studies are focused on the detection of explosives using appropriate radar signatures [15, 16]: the possibility to design metrological samples able to reproduce some particular explosive matter radar signatures could represent an interesting aid for the safety upgrade in strategic/critical environment.

This chapter is composed of three main sections. The first describes the nanocomposite materials database obtained from the dielectric characterization, by means of vector network analyzer (VNA) measurements, the mathematical modeling of the layered absorber, and the objective function optimization, used by the PSO algorithm. The second reports the main results of simulations, related to several ideal RC targets addressed; the third provides a discussion of the results based upon a FEM numerical analysis by COMSOL Multiphysics code.

2. Materials and methods

2.1. Nanocomposite materials

Several microwave reflection profiles, even having complicated shapes, have been devised to design absorbers with fitting EM responses. The proposed strategy to achieve the target behavior is to combine different components from the microwave materials database in a multilayer assembly. Such a soft approach allows to exploit a variety of dielectric properties provided by the available constituents in the materials database, as well as the characteristics of the EM field propagation, through the physical discontinuities occurring at the several layers interfaces. Polymeric composites filled with carbon nanoparticles provide an ideal platform in this framework, thanks to the possibility to explore a wide range of EM trans-
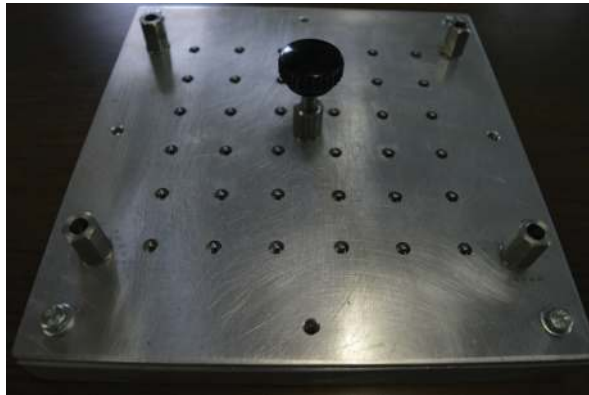
Figure 1. Sample holder used to build ring-shaped samples of nanocomposite having dimensions of 3 mm and 7 mm for inner and outer diameter respectively.

port properties, from the insulating matrix to rather conductive composites, just by tuning the nano-filler concentration within the basic polymer. A materials database of 23 carbon micro-powder- and nano-powder-filled polymeric composites has been set up and exploited. Such materials were obtained using commercial low cost products, in a well-established time-saving manufacturing procedure, in view of possible forthcoming scaling-up developments. In particular, a low-viscosity epoxy resin (Prime™ 20 LV—Gurit) was employed as polymeric matrix, while industrial grade multi-walled carbon nanotubes (MWCNT, NC7000—Nanocyl), carbon nanofibers (CNF—Sigma–Aldrich), graphene nanoplatelets (GNP, C750—XG Science), and polyaniline emeraldine base powder (PANI—Sigma–Aldrich) were added to the matrix as reinforcing materials, in different concentrations (from 0 up to 3 wt.%). The composite samples were shaped by means of an ensemble of hollow cylindrical molds (**Figure 1**) with 3 mm of internal diameter and 7 mm of the external one, as required by the specific technique adopted for the microwave characterization. The latter is based on the transmission line by means of coaxial air-line 50 Ω probe and has been carried out by means of a vector network analyzer (VNA, Agilent PNA-L N5235), via coaxial airline method in the frequency range of 2–18 GHz. The output of the measurements is obtained by means of the samples microwave reflection/transmission parameters and the materials complex electrical permittivity; the other typical dielectric properties of interest (loss tangent, skin depth, intrinsic impedance, etc.) can be then easily retrieved. The magnetic permeability of all the materials has not be taken into account during the analysis, since it is always very close to 1 (as expected for non-magnetic materials), as confirmed by the experiments. In **Figure 1**, the sample holder used to build ring samples of different reinforced materials is shown. Each hole of the sample holder is able to host the poured composite after the mixing and sonication procedures; after the curing process, the sample holder is open and the samples can be easily extracted. In **Figure 2**, the 50 Ω coaxial airline used for the VNA scattering parameters [17–19] measurements and for the subsequent computation of the relative dielectric parameters is shown: the samples are inserted around the central conductor of the coaxial airline.

Figure 2. Coaxial airline 50 Ω probe used for the dielectric characterization of nanocomposite materials and for the measurement of EM reflection and transmission properties of layered materials.
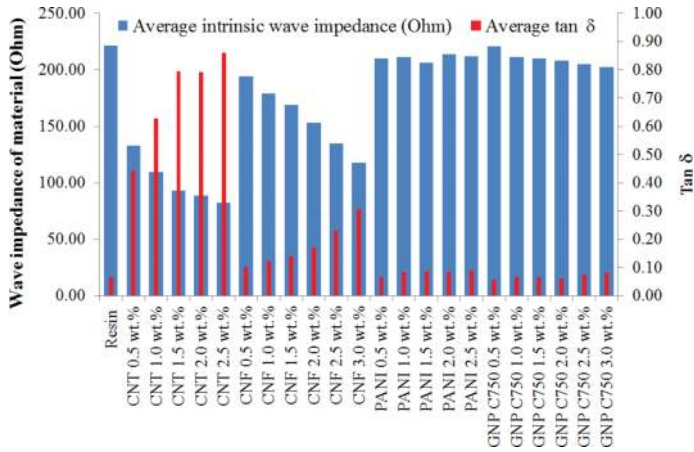

Figure 3. Loss tangent and intrinsic wave impedance of the tested nanocomposite materials in the database averaged over the frequency band 2–18 GHz.

Figure 3 shows the loss tangent and the intrinsic wave impedance of the nanocomposite materials present in the database, averaged in the frequency band 2–18 GHz. It can be seen that the CNT- and CNF-filled composites show higher EM losses and lower wave impedances, thus anticipating the employment of such materials in layers where a significant EM absorption capability is required; on the other hand, the behavior of PANI/GNP-filled

materials is similar to that of the naked resin, thus suggesting the use of such materials in impedance matching layers. The behavior of the electric permittivity of CNT-based nanocomposites is reported in **Figures 4** and **5** (real and imaginary parts, respectively). In the plots, a remarkable variation of permittivity can be observed upon variation of the CNT weight concentration, according to the change of resistive losses due to the conductive filler inclusion: such trend is more evident at lower frequencies, due to skin-depth effects. In **Table 1**, the database of materials is listed by the code number, thereafter used. In **Table 1**, the dielectric complex permittivity averaged over the microwave range investigated is also reported to allow the readers a quick idea about the materials properties. A detailed description of the materials manufacturing procedure, as well as the full database microwave characterization plotting and analysis, is available in a previously published work [20].
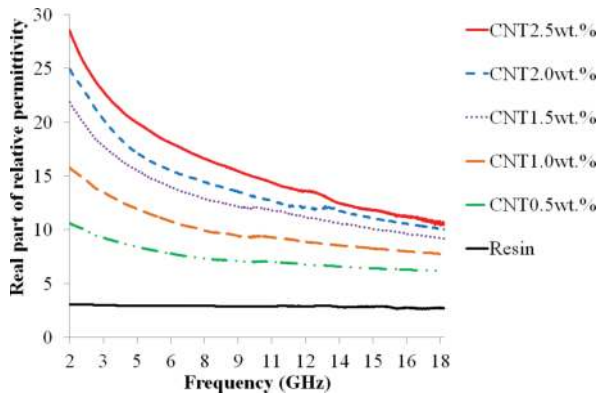

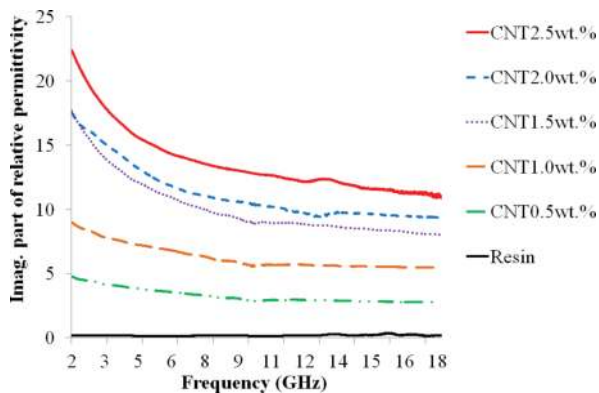**Figure 4.** Real part of permittivity of CNT-based nanocomposites.

Figure 5. Imaginary part of permittivity of CNT-based nanocomposites.

Code	Material	Average complex permittivity
1	Resin PRIME TM	2.88–j0.19
2	CNT 0.5 wt%	7.36–j3.27
3	CNT 1.0 wt%	9.98–j6.27
4	CNT 1.5 wt%	12.76–j10.14
5	CNT 2.0 wt%	14.14–j11.21
6	CNT 2.5 wt%	15.87–j13.66
7	CNF 0.5 wt%	3.74–j0.38
8	CNF 1.0 wt%	4.39–j0.53
9	CNF 1.5 wt%	4.92–j0.69
10	CNF 2.0 wt%	5.97–j1.02
11	CNF 2.5 wt%	7.57–j1.74
12	CNF 3.0 wt%	9.74–j2.99
13	PANI 0.5 wt%	3.20–j0.21
14	PANI 1.0 wt%	3.16–j0.26
15	PANI 1.5 wt%	3.31–j0.28
16	PANI 2.0 wt%	3.09–j0.26
17	PANI 2.5 wt%	3.15–j0.28
18	GNP 0.5 wt%	2.90–j0.16
19	GNP 1.0 wt%	3.17–j0.21
20	GNP 1.5 wt%	3.20–j0.20
21	GNP 2.0 wt%	3.27–j0.20
22	GNP 2.5 wt%	3.36–j0.24
23	GNP 3.0 wt%	3.44–j0.27

Table 1. Microwave composite database: materials code, composition, and complex permittivity averaged in the frequency range 2–18 GHz.

2.2. Mathematical model and objective function optimization

The multilayered EM absorber design is based on the mathematical modeling of an EM wave propagating through a sequence of slabs made of different materials. Since the goal is to reproduce a given microwave reflection profile, it is worth to remind that the reflection coefficient (RC) at an air-matter interface can be evaluated by the relationship:

$$RC_i = \left| \frac{Z_i - Z_0}{Z_i + Z_0} \right|$$

(1)

which relates the free-space impedance ($Z_0 \approx 377\ \Omega$) to the input impedance (Z_i) seen at the impinged surface for a given ith value of frequency. Such quantity depends on the dielectric properties of the material; for a multilayer structure, it is affected by multiple reflections occurring at the material interfaces and can be obtained by iterating Eq. (1) layer by layer through the formalism:

$$Z_{iu} = \eta_{iu} \frac{Z_{iu-1} \cos(k_{iu} t_u) + j\eta_{iu} \sin(k_{iu} t_u)}{\eta_{iu} \cos(k_{iu} t_u) + jZ_{iu-1} \sin(k_{iu} t_u)} \tag{2}$$

$$\eta_{iu} = \sqrt{\frac{\mu_0}{\varepsilon_0}} \sqrt{\frac{\mu_{ru}}{\varepsilon_{ru}}} \tag{3}$$

$$k_{iu}^2 = (2\pi f)^2 \mu_0 \varepsilon_0 \mu_{ru} \varepsilon_{ru} \tag{4}$$

where each layer (u) is denoted by its proper thickness (t_u) and by the EM intrinsic wave impedance (η_{iu}) of the constituent material at the ith value of frequency (f). The intrinsic wave impedance and the wave number (k_{iu}) are linked to the relative electric permittivity and magnetic permeability of the material constituting the uth layer (ε_{ru} and μ_{ru}, respectively) and to the vacuum electric permittivity and magnetic permeability (ε_0 and μ_0, respectively).

The adopted particle swarm optimization (PSO) algorithm evolves iteratively by minimizing the following objective function (*OF*):

$$OF = \sum_{frequency} \frac{|S_{RC} - T_{RC}|^2}{|S_{RC} + T_{RC}|^2} \tag{5}$$

where T_{RC} is the target RC, and S_{RC} is the simulated RC of a given multilayer—that is, a "particle" filling the space of solutions—obtained by combining Eqs. (1) and (2). Input of the design/optimization code is the target RC profile to fit and the electric permittivity of the materials in the database (the magnetic permeability is here neglected since the measurements of the dielectric parameters have shown that μ_r is unitary for all the materials under test). The output is the composition of the multilayered structure, that is, number of layers, layering sequence, and material/thickness of each layer. The PSO ranges within the space of solutions in order to minimize the *OF* defined in Eq.(4): the constraints are mainly imposed by the freedom degrees in exploring the database of available materials, in order to select the most appropriate for each layer, as well as the related thickness, limiting to a maximum of ten-layer structures. Further details on the EM wave/multilayer interaction modeling with a full description of the developed PSO algorithm can be found in some recent publications [21–23].

3. Results

The results of CEMA solutions for several RC targets are listed in **Tables 2–5**, where the target parameter, the materials of each layer coded with a number referred to **Table 1**, the thickness of each layer and the total thickness of the multilayer are reported. All the solutions are represented as ten-layer sequences: of course, a zero thick layer means that the PSO algorithm optimized the final layered material without the necessity of using that particular layer. In some cases, the indication of the PSO parameter α is also provided [21–23], whose meaning is here briefly recalled: by this parameter, the OF optimization is weighted with respect to the multilayer total thickness (e.g., $\alpha = 1$ means that only OF will be taken into account by PSO, without taking care of the thickness minimization). In the next **Figures 6–15**, the plot of the RC simulations is reported, comparing to the corresponding targets (red dashed lines). Almost all the simulations are based on RC target imitation by providing a PEC at the end of the layered material, except two. In particular, CEMA 02 has been designed providing free-space environment on both sides, that is, without the presence of PEC as the back-end of the structure. For CEMA 24, two different design scenarios have been taken into account: the first one represents the usual RC target imitation with a PEC-backed multilayer, while the second one explores the possibility to consider the TC as target parameter to be assigned to the PSO algorithm, thus requiring free space at both sides (here the other PSO parameter γ is introduced, to point out the weight in RC/TC addressing: $\gamma = 0$ indicates the RC optimization with no regard to TC, vice versa for $\gamma = 1$, intermediate values represent an optimization process that takes into account for TC and RC imitation simultaneously—cfr. CEMA02 plot). In this special case, the expected EM losses phenomena within the material increase with the frequency, thus progressively lowering down the TC values: such unwanted collateral effect is unavoidable since the higher the frequency the greater the skin-depth effect, which in turns increases the EM wave losses within thick materials.
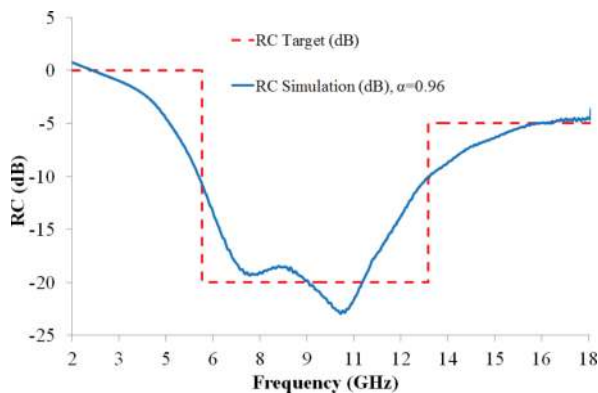

Figure 6. Plot of CEMA 00.

Target	CEMA	Materials	Layers thickness (mm)	Total thickness (mm)
T_{RC} 00	CEMA 00	18	4.5966	6.7069
		6	0	
		6	1.3962	
		2	0.4814	
		7	0.2162	
		10	0	
		18	0	
		13	0	
		5	0.0166	
		9	0	
		PEC	–	
T_{RC} 02	CEMA 02	17	0.6711	41.5812
		18	2.1669	
		12	3.4105	
		10	0	
		8	9.0000	
		19	1.1553	
		10	9.0000	
		13	0	
		7	9.0000	
		17	7.1774	
		Free space	–	
T_{RC} 13	CEMA 13 ($\alpha = 0.96$)	15	2.6898	44.1832
		11	1.2257	
		9	0.0798	
		11	9.0000	
		8	3.9273	
		3	8.2297	
		10	8.1644	
		12	9.0000	
		10	1.4261	

Target	CEMA	Materials	Layers thickness (mm)	Total thickness (mm)
		3	0.4403	
		PEC	–	
T_{RC} 13	CEMA 13 ($\alpha = 0.99$)	11	0.0603	48.0260
		7	2.4181	
		12	9.0000	
		16	4.4037	
		7	0	
		11	0.6423	
		12	9.0000	
		15	9.0000	
		12	9.0000	
		12	4.5016	
		PEC	–	

Table 2. CEMA solutions by PSO for different target: layers sequence (materials coded as in **Table 1**), single layers, and total multilayer thickness.

Target	CEMA	Materials	Layers thickness (mm)	Total thickness (mm)
T_{RC} 15	CEMA 15 ($\alpha = 0.99$)	1	8.5696	44.8402
		11	0	
		9	9.0000	
		18	4.9133	
		10	8.7613	
		12	0.6217	
		11	0.5130	
		6	9.0000	
		12	3.4488	
		17	0.0125	
		PEC	–	
T_{RC} 15	CEMA 15 ($\alpha = 0.96$)	21	0	30.0380
		1	8.6290	
		12	0	

Target	CEMA	Materials	Layers thickness (mm)	Total thickness (mm)
		11	0	
		8	0.0046	
		8	0.4763	
		10	7.8559	
		10	0	
		16	4.7368	
		2	8.3354	
		PEC	–	
T$_{RC}$ 16	CEMA 16 ($\alpha = 0.96$)	19	9.0000	16.7440
		12	0	
		9	0	
		15	2.9726	
		5	2.0314	
		13	0	
		10	2.7400	
		13	0	
		16	0	
		14	0	
		PEC	–	
T$_{RC}$ 16	CEMA 16 ($\alpha = 0.99$)	15	9.0000	46.9286
		6	0	
		22	3.2445	
		12	1.3837	
		15	8.8354	
		12	9.0000	
		10	9.0000	
		12	3.3121	
		15	0	
		17	3.1529	
		PEC	–	

Table 3. CEMA solutions by PSO for different target: layers sequence (materials coded as in **Table 1**), single layers, and total multilayer thickness.

Target	CEMA	Materials	Layers thickness (mm)	Total thickness (mm)
T_{RC} 17	CEMA 17 ($\alpha = 0.99$)	18	6.7023	52.3048
		8	4.4908	
		11	0	
		12	9.0000	
		10	0.5107	
		10	9.0000	
		12	1.1707	
		11	3.4329	
		6	9.0000	
		14	8.9974	
		PEC	–	
T_{RC} 17	CEMA 17 ($\alpha = 0.96$)	18	5.7320	37.2708
		5	0	
		7	1.5600	
		5	0	
		10	2.9788	
		4	9.0000	
		10	0	
		7	0	
		14	9.0000	
		14	9.0000	
		PEC	–	
T_{RC} 20	CEMA 20 ($\alpha = 0.96$)	18	6.8693	33.4005
		2	0	
		10	4.4797	
		3	6.7434	
		14	3.1642	
		14	9.0000	

Target	CEMA	Materials	Layers thickness (mm)	Total thickness (mm)
		6	1.3522	
		11	0	
		13	0	
		21	1.7917	
		PEC	–	
T_{RC} 20	CEMA 20 (α = 0.99)	18	2.5959	44.5547
		15	4.1778	
		8	0.0476	
		8	0	
		12	0.3846	
		10	3.8949	
		11	9.0000	
		11	9.0000	
		12	8.9970	
		4	6.4568	
		PEC	–	

Table 4. CEMA solutions by PSO for different target: layers sequence (materials coded as in **Table 1**), single layers, and total multilayer thickness.

Target	CEMA	Materials	Layers thickness (mm)	Total thickness (mm)
T_{RC} 23	CEMA 23 (α = 0.99)	13	9.0000	82.1359
		18	9.0000	
		21	7.1326	
		18	6.4060	
		13	9.0000	
		17	7.8792	
		18	7.8883	
		13	8.8366	
		13	9.0000	

Target	CEMA	Materials	Layers thickness (mm)	Total thickness (mm)
		13	7.9931	
		PEC	–	
T_{RC} 24	CEMA 24 only TC ($\alpha = 0.99$, $\gamma = 0$)	20	8.5429	25.5742
		13	0	
		8	4.9744	
		14	9.0000	
		6	2.0820	
		14	0	
		9	0	
		19	0.9749	
		13	0	
		18	0	
		Free-space	–	
T_{TC} 24	CEMA 24 only RC ($\alpha = 0.99$, $\gamma = 1$)	20	9.0000	48.9902
		22	9.0000	
		8	9.0000	
		9	0.1918	
		4	1.8001	
		12	9.0000	
		13	0	
		13	9.0000	
		13	1.9983	
		12	0	
		PEC	–	

Table 5. CEMA solutions by PSO for different target: layers sequence (materials coded as in **Table 1**), single layers, and total multilayer thickness.

The PSO algorithm shows an intriguingly effective mimic capability in almost all the cases, even for the most demanding (actually "not physical") targets conceived. Of course, the reliability degree is strictly linked to the target shape, that is, to the peaks number and depth as well as to the sharpness of the RC variations to be hunted. T_{RC} 00 and T_{RC} 02 present a simple filter-shaped profile: the corresponding solutions are able to broadly follow the target trend, even if the sharp (ideal) square-like behavior, with deep peaks up to 20 dB, does not allow a satisfactory imitation around the edges. In particular, CEMA 02 almost loses track of the target at the frequency range boundaries, probably due to the TC weighting in this free-space backed situation. Other regular square-like target profiles (multi-filter behavior) with RC oscilla-

tions of about 15 dB confirm both potentialities and issues of the method. In particular, the very difficult task of T_{RC} 23 imitation is actually impossible to tackle, even if the quasi-total reproduction of all the oscillating peaks by CEMA 23 represents a surprising result in this case. T_{RC} 16 is much easier to be imitated due to the greater peaks width, even if some inaccuracies are discovered for both the CEMA 16 solutions at lowest frequencies. The results obtained by CEMA 24 can be seen as intermediate case of the latter two. An excellent mimic effectiveness is provided by CEMAs 15, 17, and 20, which are able to closely follow the corresponding targets: in such cases, the algorithm is "aided" by the lower peaks depth and mainly by smoother RC variations in frequency. The difference in pursuing triangle-shaped *versus* square-shaped RC oscillations is well established by the two CEMA 13 solutions, which alternatively match and miss the exotic "stair-profile" of T_{RC} 13. For the T_{RC} 13, 15, 16, 17, and 20, two CEMA solutions have been proposed by slight variation of α. It can be noticed that at lower α (0.96) the algorithm finds solutions with thinner total thickness: that is reflected by the simulations, which shows a little bit more inaccuracy (black dashed lines) around the sharpest RC variations. Concerning the transmission targets ($\gamma \neq 0$), difficulty to conceive appreciable solutions in such framework due to the abovementioned intrinsic skin-depth effects, evident in both the situations investigated, needs to be pointed out. In T_{RC} 02, the parameter γ is set to 0.5 (i.e., the optimization of RC and TC is equally weighted) and a constant low transmission rate is defined: besides the loss effects, the simultaneous research of a layering to follow the RC target leads to an intermediate solution, not suitable for the required transmission (otherwise a quasi-full absorbing structure would have been identified). As for the T_{TC} 24 ($\gamma = 1$), a challenging square-shaped transmission profile is defined (by analogy with T_{RC} 24, $\gamma = 0$). The quite fast target oscillations are only remotely hinted by the CEMA 24 solution, whose average TC substantially decreases at higher frequency; nevertheless, it is worth noticing that the corresponding reflection presents a peaks series roughly reversed, in respect to the transmission target.
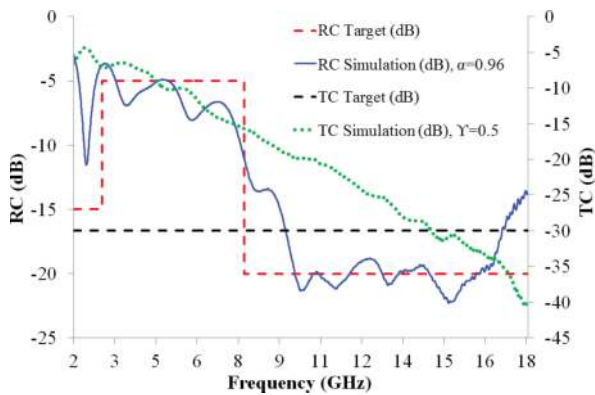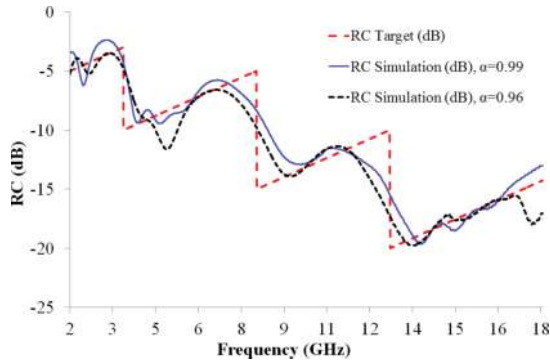

Figure 7. Plot of CEMA 02.

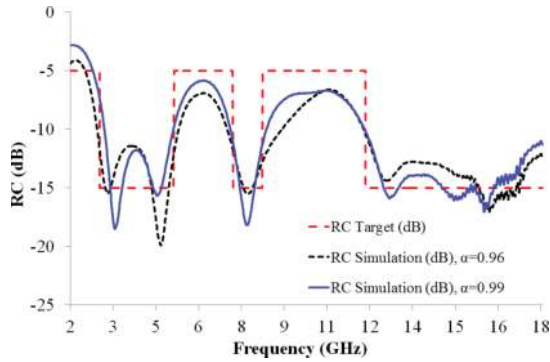**Figure 8.** Plot of CEMA 13.

Figure 9. Plot of CEMA 15.

A promising level of confidence is suggested from the reported results in each phase of the work, from the database materials preliminary characterization to the mathematical modeling of the EM field/matter interaction, up to the PSO algorithm design optimization. The capability of the layering approach lies in the frequency selective interaction between the different materials and the EM field. Such concept is well explained by a finite element method (FEM) simulation where CEMA13 (α = 0.96) has been deeply analyzed by studying the multilayer structure inserted in a 50 Ω coaxial airline of the same type used to measure the dielectric properties of the database materials. The FEM analysis shows how the EM field propagates through the several layers at two different frequencies, 2.5 and 14 GHz, where the reflection coefficient, respectively, results maximum and minimum. Commercial code COMSOL Multiphysics has been used for the FEM analysis [20, 24]. In **Figure 16**, the mesh of the multilayer within the coaxial waveguide is depicted: the blue part on the left is the empty section of the airline, while the other is the part filled with ten layers of nanocomposite materials. The airline is simulated using a perfect electric conductor for inner, outer, and back
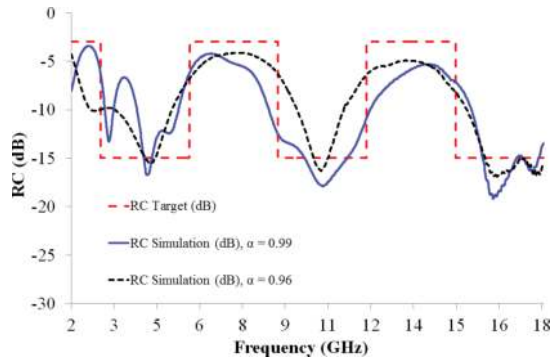
Figure 10. Plot of CEMA 16.

surfaces. The Port1 is placed at the beginning of the coaxial airline on the left side of the figure. The maximum element size of the mesh is 1/10 of the minimum EM wavelength ($\lambda = 3 \times 10^8/f_{max} \sim 1.6$ cm), while the minimum element size of the mesh is in the order of 10^{-7} m: these dimensions enable an optimal growth of the mesh and guarantee the needed accuracy in the EM analysis. In the coaxial airline, Port 1 is used to compute the scattering parameter S_{11}, related to the reflection coefficient. In the numerical simulation, the power set at the port is 3 dBm (2 mW) as in the real measurement. All the parameters adopted to run the FEM simulation are chosen in such a way to reproduce the experimental conditions of the microwave characterization. In particular, the real and imaginary part of the complex electrical permittivity measured over the 2–18 GHz frequency band to create the database of nanocomposite materials have been adopted: such values are interpolated by COMSOL code in order to get out a functional relationship between dielectric properties and frequency. The EM interfaces of the code cover the modeling of EM fields and waves in the frequency domain, formulating and solving the differential form of Maxwell's equations together with the initial and boundary conditions.
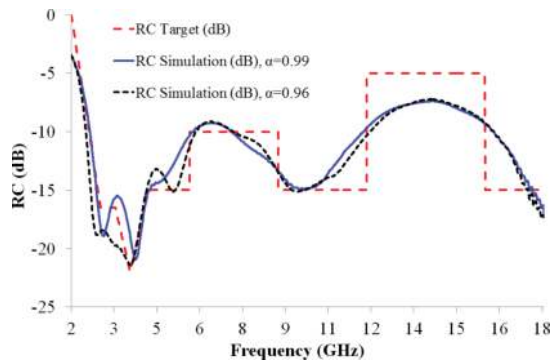
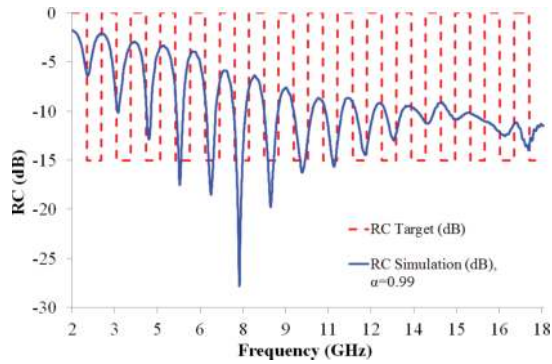**Figure 11.** Plot of CEMA 17.
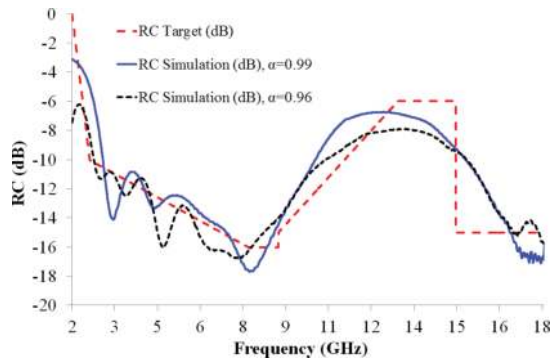
Figure 12. Plot of CEMA 20.
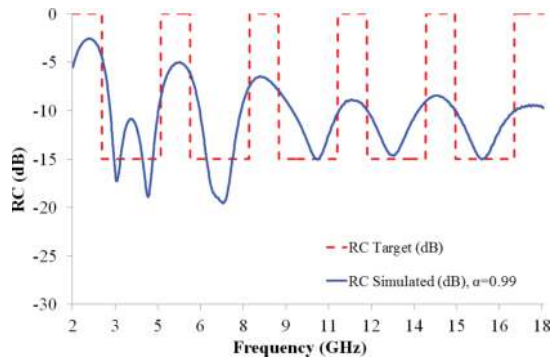

Figure 13. Plot of CEMA 23.

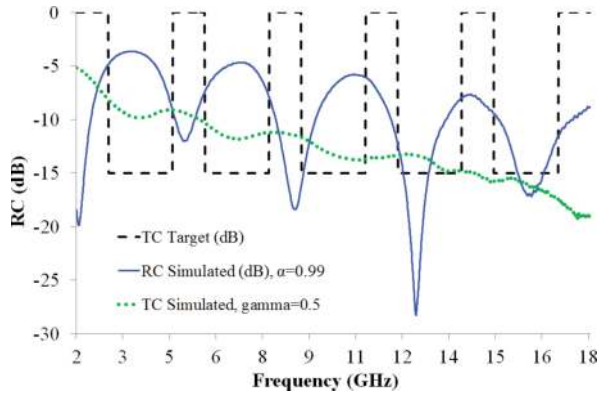**Figure 14.** Plot of CEMA 24, optimization of RC.
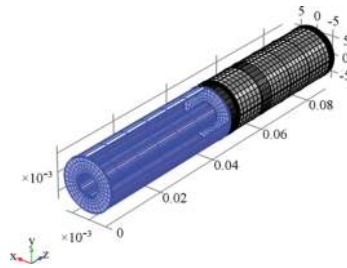
Figure 15. Plot of CEMA 24, optimization of TC.

Figure 16. Mesh of the CEMA 13 ($\alpha = 0.96$), ten-layered structure in the coaxial airline setup.

In **Figures 17** and **18**, the electric field (V/m) is reported at 2.5 and 14 GHz respectively. In **Figures 19** and **20**, the current density (A/m^2) arrow lines and magnetic field (A/m) circular lines for the ten layers of CEMA13 are shown (arrow lines are used to show the region where the highest EM losses occur along the structure). In **Figures 21** and **22**, the power loss density (W/m^3) at 2.5 and 14 GHz, respectively, is shown. At 14 GHz, the multilayer design provides the impedance matching with free space, thus resulting in a higher level of EM absorption, as compared to the values of the electric field at 2.5 GHz. Alongside, the significant current density at 14 GHz is well visible in the first and second layers, whereas at 2.5 GHz the impedance mismatch causes a great reflection of the EM field at the first layer, thus determining a lower power loss within the deep bulk. In fact, the power loss density at 2.5 GHz is quite lower compared to the value obtained at 14 GHz, where geometrically power losses are mainly confined within the 5 first layers. In other words, at 2.5 GHz, the EM field propagates through all the layers due to the impedance mismatch end. Due to the higher value of the reflection coefficient, the majority of the power is reflected back at the first air-multi-layer interface. At 14 GHz, the multilayer is impedance matched, the reflection coefficient is quite lower and the absorbed power dramatically increases. In **Figure 23**, a comparison

between the RC Target, RC simulated with mathematical model and RC simulated by FEM analysis is shown. The discrepancies with FEM simulation are due to the mesh and the approximation of the EM field solution, which is more difficult at high frequencies.
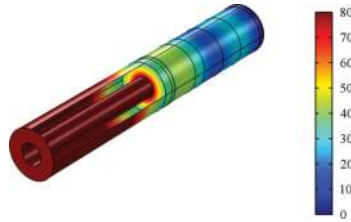

Figure 17. Electric field (V/m) at 2.5 GHz.
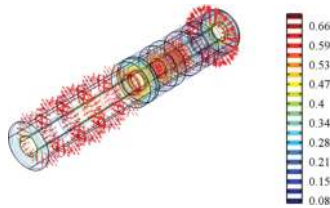

Figure 18. Electric field (V/m) at 14 GHz.

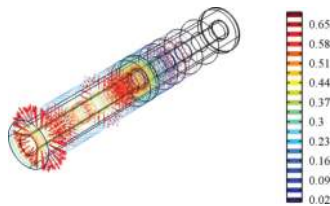**Figure 19.** Magnetic field (A/m) circular line and current density (A/m^2); red arrow lines at 2.5 GHz.

Figure 20. Magnetic field (A/m) circular line and current density (A/m^2); red arrow lines at 14 GHz.

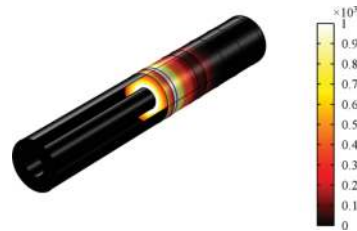**Figure 21.** Power loss density (W/m^3) at 2.5 GHz.

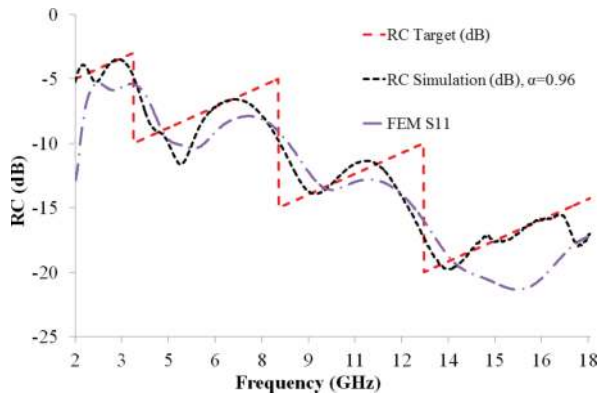**Figure 22.** Power loss density (W/m^3) at 14 GHz.

Figure 23. Comparison of RC Target, RC simulated, and RC simulated with FEM.

4. Conclusions

In this chapter, an attempt to identify a novel approach to design and optimize EM reference materials for metrological applications was introduced. The results highlight the intriguing potentialities of the proposed strategy, since even hard microwave reflection target profiles

are successfully addressed by the numerical design optimization technique developed. It is clear that several upgrades can be introduced in order to better refine the process. The above mentioned examples highlight some root of inaccuracy, especially when quite sharp edges occur along the target profile. Of course, the harder it is to follow a given profile, the more complex the optimized structure will become out in terms of layers number and thinness. Although the intriguing capability of the PSO algorithm to find solutions fitting such challenging targets, it has to be outlined that the corresponding CEMA solutions are composed by at least four layers (almost always six or more), with total thickness over 4 cm, in the most of the situations. Furthermore, quite often the layers that fulfill the crucial EM absorbing role have thickness well below 1mm, thus pointing out that an eventual production process could represent a big task in this framework. Beyond possible PSO algorithm enhancements (convergence parameters, particles population, iterations), the effectiveness of the proposed strategy in terms of mimic capability would be significantly improved by enriching the materials database. The possibility to draw on a "quasi-continuous" spectrum of dielectric properties should allow the PSO algorithm to find solutions for reproducing any RC profile even more faithfully. On the other hand, by proper constraints in terms of layers number and thickness, the increased availability of materials should make the algorithm able to identify multilayered combinations easy to be practically achieved. In this respect, the employment of composites reinforced with nanoparticles sounds as the right way forward. With respect to the conventional materials, in fact, the family of nano-filled composites allows the unique opportunity to finely adjust the EM absorption property just by tuning the weight percentage of the nanofiller within the matrix. At this purpose, the lower the incremental step in weight percentage, the greater the possibility of fine tuning: thus, the greater the database population, the better the possibility to select appropriate materials for mimic purposes. The research development will thus be addressed to enrich the database population, in order to obtain even more precise and feasible solutions for the widest variety of electromagnetic requirements.

Author details

Davide Micheli[*], Roberto Pastore, Antonio Vricella and Mario Marchetti

*Address all correspondence to: davide.micheli@uniroma1.it

Astronautic Electric and Energy Engineering Department, Sapienza University of Rome, Rome, Italy

References

[1] Sheffield RG, The official F-19 stealth fighter handbook, Radnor, Pennsylvania: Pam Williams ed, 1989. ISBN 10: 0874552176: 1–184.

[2] Knott EF, Shaeffer J, Tuley M, Radar cross section, 2nd edn, SciTech Publishing Inc., 2004: 112–115.

[3] Mosallaei H, Rahmat-Samii Y. RCS reduction of canonical targets using genetic algorithm synthesized RAM. IEEE Trans. Antennas Propag. 2000; 48(10): 1594–1606. doi:10.1109/8.899676

[4] Vinoy KJ, Jha RM, Radar absorbing materials—from theory to design and characterization. Boston: Kluwer, 1996. ISBN 978-1-4613-8065-8: 1–173.

[5] Sagalianov IY, Vovchenko LL, Matzui LY, Lazarenko AA, Oliynyk VV, Lozitsky OV, Ritter U. Optimization of multilayer electromagnetic shields: A genetic algorithm approach. Mat.-wiss. u. Werkstofftech. 2016. doi:10.1002/mawe.201600483.

[6] Micheli D, Apollo C, Pastore R, Marchetti M. X-band microwave characterization of carbon-based nanocomposite material, absorption capability comparison and RAS design simulation. Composites Sci. Technol. 2010; 70(2): 400–409. doi:10.1016/j.compscitech.2009.11.015

[7] Li N, Huang Y, Du F, He X, Lin X, Gao H, Ma Y, Li F, Chen Y, Eklund PC. Electromagnetic interference (EMI) shielding of single-walled carbon nanotube epoxy composites. Nano Lett. 2006; 6(6): 1141–1145. doi:10.1021/nl0602589

[8] Chang CM, Chiu JC, Jou WS, Wu TL, Cheng WH. New package scheme of a 2.5-Gb/s plastic transceiver module employing multiwall nanotubes for low electromagnetic interference. IEEE J. Select. Top. Quantum Electron. 1989; 25(5): 1025–1031. doi:10.1109/JSTQE.2006.879534

[9] Bogush V, Borbotko T, Kolbun N, Lynkov L. Novel composite shielding materials for suppression of microwave radiation. In: International conference on microwaves radar wireless communications, 2006. MIKON 2006. 645–647. doi:10.1109/MIKON.2006.4345262

[10] Emerson W. Electromagnetic wave absorbers and anechoic chambers through the years. IEEE Trans. Antennas Propag. 1973; AP-21(4): 484–490. doi:10.1109/TAP.1973.1140517

[11] Holloway CL, DeLyser RR, German RF, McKenna P, Kanda M. Comparison of electromagnetic absorber used in anechoic and semi-anechoic chambers for emissions and immunity testing of digital devices. IEEE Trans. Electromagn. Compat. 1997; 39(1): 33–47. doi:10.1109/15.554693

[12] Davide Micheli, Roberto Pastore, Gabriele Gradoni and Mario Marchetti. Tunable nanostructured composite with built-in metallic wire-grid electrode. AIP Adv. 2013; 2158–3226/3(11): 112132–112137. doi:10.1063/1.4837916

[13] Meissner T, Wentz FJ. The complex dielectric constant of pure and sea water from microwave satellite observations. IEEE T. Geosci. Remote 2004. 42, 1836–1849. doi:10.1109/TGRS.2004.831888

[14] Hoeben R, Troch PA. Assimilation of active microwave observation data for soil moisture profile estimation. Water Resour. Res. 2000; 36, 2805–2819. doi: 10.1029/2000WR900100

[15] Martinez-Lorenzo JA, Rappaport C, Sullivan R, Angell A. Standoff concealed explosives detection using millimeter-wave radar to sense surface shape anomalies. Antennas and Propagation Society International Symposium, 2008. AP-S 2008. IEEE. pp 1–4. doi:10.1109/APS.2008.4619051

[16] Robert J, Douglass J, Gorman D, Burns TJ. System and method for standoff detection of human carried explosives. Patent US 7800527 B2, PCT/US2005/036593, 2010.

[17] Micheli D, Apollo C, Pastore R, Marchetti M. Modeling of microwave absorbing structure using winning particle optimization applied on electrically conductive nanostructured composite material. 19th ICEM 2010, Rome (IT) 2010; ISBN 978-1-4244-4174-7: 1–10. doi:10.1109/ICELMACH.2010.5607881

[18] Micheli D, Pastore R, Marchetti M, Gradoni G, Moglie F, Mariani Primiani V. Modeling and measuring of microwave absorbing and shielding nanostructured materials. IEEE EMC Europe 2012, Rome (IT) 2012; ISBN 978-1-4673-0718-5: 1–5. doi:10.1109/EMCEurope.2012.6396810

[19] Micheli D, Radar absorbing materials and microwave shielding structure design, LAP Lambert Academic Publishing 2012; ISBN 978-3-8465-5939-0: 334–446.

[20] Micheli D, Vricella A, Pastore R, Marchetti M. Synthesis and electromagnetic characterization of frequency selective radar absorbing materials using carbon nanopowders. Carbon 2014; 77: 756–774. doi:10.1016/j.carbon.2014.05.080

[21] Micheli D, Pastore R, Gradoni G, Mariani Primiani V, Moglie F, Marchetti M. Reduction of satellite electromagnetic scattering by carbon nanostructured multilayers. Acta Astron 2013; 88: 61–73. doi:10.1016/j.actaastro.2013.03.003

[22] Micheli D, Pastore R, Apollo C, Marchetti M, Gradoni G, Mariani Primiani V, Moglie F. Broadband electromagnetic absorbers using carbon nanostructure-based composites. IEEE Trans. Microwave Theory Tech. 2011; 59(10): 2633–2646. doi:10.1109/TMTT.2011.2160198

[23] Micheli D, Apollo C, Pastore R, Barbera D, Bueno Morles R, Marchetti M, Gradoni G, Mariani Primiani V, Moglie F. Optimization of multilayer shields made of composite nanostructured materials. IEEE Trans. Electromagn. C 2012; 54(1): 60–69. doi:10.1109/TEMC.2011.2171688

[24] Pryor RW. Multiphysics modeling using COMSOL: a first principles approach. Sudbury: Jones & Bartlett Learning; 2009.